International Journal of Pharmaceutics 665 (2024) 124700

Contents lists available at ScienceDirect

International Journal of Pharmaceutics

journal homepage: www.elsevier.com/locate/ijpharm

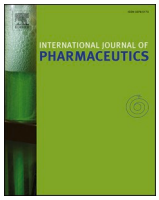

Development of dual drug loaded-hydrogel scaffold combining microfluidics and coaxial 3D-printing for intravitreal implantation

Elide Zingale [a,b], Edward Weaver [a], Pietro Maria Bertelli [c], Imre Lengyel [c], Rosario Pignatello [b,*], Dimitrios A. Lamprou [a,*]

[a] School of Pharmacy, Queen's University Belfast, 97 Lisburn Road, Belfast BT9 7BL, UK
[b] Laboratory of Drug Delivery Technology, Department of Drug and Health Sciences, University of Catania, Viale A. Doria, 6, 95125 Catania, Italy
[c] Wellcome-Wolfson Institute for Experimental Medicine, School of Medicine, Dentistry and Biomedical Science, Queen's University Belfast, Belfast, Northern Ireland, UK

ARTICLE INFO

Keywords:
Hydrogel
Biodegradable implant
Intravitreal
Liposomes
3D-printing
Microfluidics
Hyaluronic acid
Chitosan
Sustained release
Diabetic retinopathy

ABSTRACT

Treating diabetic retinopathy (DR) effectively is challenging, aiming for high efficacy with minimal discomfort. While intravitreal injection is the current standard, it has several disadvantages. Implantable systems offer an alternative, less invasive, with long-lasting effects drug delivery system (DDS). The current study aims to develop a soft, minimally invasive, biodegradable, and bioadhesive material-based hydrogel scaffold to prevent common issues with implants. A grid-shaped scaffold was created using coaxial 3D printing (3DP) to extrude two bioinks in a single filament. The scaffold comprises an inner core of curcumin-loaded liposomes (CUR-LPs) that prepared by microfluidics (MFs) embedded in a hydrogel of hydroxyethyl cellulose (HEC), and an outer layer of hyaluronic acid-chitosan matrix with free resveratrol (RSV), delivering two Sirt1 agonists synergistically activating Sirt1 downregulated in DR. Optimized liposomes, prepared via MFs, exhibit suitable properties for retinal delivery in terms of size (<200 nm), polydispersity index (PDI) (<0.3), neutral zeta potential (ZP), encapsulation efficiency (~97 %), and stability up to 4 weeks. Mechanical studies confirm scaffold elasticity for easy implantation. The release profiles show sustained release of both molecules, with different patterns related to different localization of the molecules. RSV released initially after 30 min with a total release more than 90 % at 336 h. CUR release starts after 24 h with only 4.78 % of CUR released before and gradually released thanks to its internal localization in the scaffold. Liposomes and hydrogels can generate dual drug-loaded 3D structures with sustained release. Microscopic analysis confirms optimal distribution of liposomes within the hydrogel scaffold. The latter resulted compatible *in vitro* with human retinal microvascular endothelial cells up to 72 h of exposition. The hydrogel scaffold, composed of hyaluronic acid and chitosan, shows promise for prolonged treatment and minimally invasive surgery.

1. Introduction

Diabetes is a prevalent global problem, with an estimated 12 % of the adult population aged 20–79 years-old worldwide expected to be affected by 2045. Diabetic retinopathy (DR), a frequent complication of diabetes, is projected to affect an increased population of 642 million by 2050 (Abou Taha et al., 2024). DR is defined as a microvascular and neurodegenerative disease involving oxidative stress and inflammatory conditions. Metabolic dysfunction related to lipids and glucose leads to accumulation of reactive oxygen species (ROS), leukocyte activation, angiogenesis, and microvascular complications (Leley et al., 2021). The gold standard treatment for this pathology is the intravitreal injection of anti-VEGF agents. However, numerous drawbacks are associated with this administration, including non-adherence and lack of persistence to therapy, poor patient compliance, the need for repeated injections, sustained elevation of intraocular pressure after injections, corneal oedema, and a high risk of endophthalmitis (Cui et al., 2019; Forrester et al., 2020; Liu et al., 2023). Despite the safety and high compliance of non-invasive methods such as topical administration, the drug bioavailability in the aqueous vitreous humor is generally less than 3 % after instillation (Sigford et al., 2015). This is primarily due to poor bioavailability of the molecules. This is caused by the presence of highly selective barriers, such as the corneal epithelium, conjunctiva, sclera, and the choriocapillaris, as well as the rapid drainage of the formulation

* Corresponding authors.
E-mail addresses: rosario.pignatello@unict.it (R. Pignatello), D.Lamprou@qub.ac.uk (D.A. Lamprou).

https://doi.org/10.1016/j.ijpharm.2024.124700
Received 4 July 2024; Received in revised form 8 September 2024; Accepted 10 September 2024
Available online 13 September 2024

into the nasolacrimal system, due to dynamic barriers, such as lacrimation, blinking, conjunctival hyperaemia, and conjunctival absorption into the systemic circulation (Farkouh et al., 2016; Naageshwaran et al., 2022). These factors make targeting drugs to the posterior eye a challenging task.

Implants have received much attention as they allow for extended drug release, reduce the need for repeated administration, increase patient compliance, they are suitable for sterilization, and provide a defined and proper concentration of the drug directly at the site of administration. An increasing number of implants are now available in the market. Among them, Vitrasert® was the first and is a non-biodegradable implant. This was part of the first generation of implants, along with Illuvien®, Retisert®, and Durasert®. The second generation includes biodegradable implants such as Ozurdex® (Cao et al., 2019; Jervis, 2017).

Compared to biodegradable implants, non-biodegradable implants have some drawbacks, as they require surgical insertion and removal, often through invasive procedures. Additionally, they can cause anterior chamber migration, leading to corneal oedema and corneal decompensation, as well as an increased incidence of post-operative cataracts (Khurana et al., 2014).

Biodegradable scaffolds do not require surgical removal; thus, despite their shorter lifespan compared to non-biodegradable ones, they can ensure greater patient comfort and compliance. Within this category, hydrogel implants offer the advantages of being softer, usefully flexible for repositioning, and causing less discomfort. The main purpose of the current study is to develop a highly biocompatible hydrogel scaffold, made of biodegradable, highly biocompatible and bioadhesive materials to prevent anterior chamber migration (Barth et al., 2016; Rafael et al., 2023; Tan et al., 2022). The hydrogel scaffolds were prepared using hyaluronic acid (HA) and chitosan (CS) by a 3D bioprinting approach.

HA is widely used in the formation of bioinks, and often functionalized to improve its mechanical properties and slow its degradation. HA is endogenous to the body and is non-immunogenic. Specifically, in the eye, it constitutes a major component of the vitreous body (at concentrations of 140–340 μg/ml) along with collagen and it has ligands for receptors found in many types of retinal cells, such as CD-44 (Mishra et al., 2023; Zhang et al., 2021). Despite the aim of formulating a hydrogel based on HA to be as compatible as possible with the target site for intravitreal implantation, its poor mechanical properties and rapid degradation in vivo are significant disadvantages and must be considered. The use of chitosan to prepare a polyelectrolyte complex (PEC) with HA is a widely used strategy in the literature (Barroso et al., 2019; Drozdova et al., 2022; Khoonkari et al., 2023; Maiz-Fernández et al., 2021). It serves as a secondary material aimed at forming an oppositely charged PEC with HA, thereby enhancing its mechanical properties, rendering HA mouldable, and increasing the bioadhesion of the system (Amato et al., 2020; Li et al., 2014). The combination of two materials is used to form bioink, but mostly both materials, in particular HA is modified to allow the printing. Our work proposes a formation of bioink without modification of polymers that resulted a challenge for printing approach. Moreover, no studies in literature investigate the combination of HA and CS for preparation of 3D printing hydrogel scaffold addressed to the intravitreal implantation. A challenge is the printability of this mixture reported as a difficult step. The aim to use CS lies in adhesive properties with various mucous tissues and, owing to its positive charge, can bind the negatively charged polymer network of vitreous humor, primarily due to the presence of heparan sulfate. Polymers with cationic properties could enhance tissue adhesion, thereby prolonging permanence and preventing the typical disadvantage of anterior chamber system migration associated with many implants. The use of coaxial 3D printing allows to the constitution of system for delivery of two compound at a time with different localization: one in the inner core and one in the shell. This approach resulted a strategy not yet investigated in the ocular field.

Lipid-based nanoparticles (NPs) have been investigated as a compelling strategy to enhance the solubility and bioavailability of drugs with low water solubility, regulate release kinetics, increase apparent solubility in water, boost drug loading, and reduce ocular clearance (Chaw et al., 2021; Moiseev et al., 2022). Among these, liposomes have garnered significant attention for ocular administration due to their pronounced biocompatibility and low cytotoxicity. Particularly, pegylated liposomes have demonstrated success in overcoming vitreal barriers, improving retinal targeting, stability, and retention in the retinal tissue (Tavakoli et al., 2020). Given the advantages associated with liposomes, this study aims to deliver a Sirt1 agonist molecule via a biodegradable implant. By combining two techniques, microfluidics (MFs) and coaxial 3DP, it becomes feasible to deliver two molecules with Sirt1 agonist properties simultaneously, enhancing synergistic effects and exploring potential differences in behaviour between the internal and external matrices, as recently investigated by Fratini et al., for wound healing treatments (Fratini et al., 2023). Coaxial 3DP offers the advantage of creating an internal core capable of housing a hydrogel embedded with liposomes, thus delivering, and protecting, one molecule inside, while also forming an external shell composed of HA/CHI matrix embedded with a second molecule. Importantly, MFs and 3DP are both environmentally friendly and economically viable approaches (Weaver et al., 2022).

Several studies demonstrate a correlation between the downregulation of Sirt1 and DR. This protein plays a cytoprotective role in ocular tissues such as the retina and the optic nerve. Downregulation leads to increased susceptibility of these tissues to degenerative disorders (Hammer et al., 2021). Polyphenolic compounds function as activators of Sirt1, enhancing its activity by reducing the Michaelis constant (Km) of its substrates, i.e. the substrate concentration at which an enzyme is half saturated, which leads to a small amount of substrate being required to saturate the enzyme. Recent studies indicate that compounds such as resveratrol, curcumin, berberine, quercetin, and others act as agonists of this protein (Wiciński et al., 2023). However, their therapeutic efficacy is hindered by low solubility in aqueous environments, limited bioavailability, degradation in various environments, and instability over time (Wiciński et al., 2023). Resveratrol (RSV) stands out as the most potent activator of Sirt 1in retinal cells, as it allosterically binds to Sirt1 and reduces the Michaelis constant of Sirt1 for acetylated substrate (Cao et al., 2020). Therefore, RSV has been designated for incorporation into the outer hydrogel matrix. Curcumin (CUR), a polyphenolic compound with Sirt1 activator properties, is extensively studied in the field of eye treatment and theranostics. A water-soluble fraction of CUR at a low concentration (5 μM) induces a cytoprotective effect in retinal cells exposed to oxidative stress (Nedzvetsky et al., 2021). CUR also serves as an anti-VEGF agent, beneficial for treating neovascularization in proliferative diabetic retinopathy (Jiang et al., 2023). Encapsulating CUR inside liposomes enhances its protection and stability (Ballacchino et al., 2021). When RSV and CUR are used together, they exhibit increased antidiabetic and antioxidant effects. The combination of RSV and CUR leads to a greater reduction in plasma glucose levels compared to either molecule alone. Additionally, as hyperglycaemia exacerbates oxidative stress by increasing reactive oxygen species (ROS) production, the combination of RSV and CURC elevates levels of glutathione (GSH) and superoxide dismutase (SOD) compared to individual molecules (Hussein and El-Maksoud, 2013). The development of a hydrogel scaffold prepared through a combination of microfluidics and coaxial 3DP, which simultaneously loads two molecules, represents a novel approach in the ocular field since no studies with the same aim are present in the literature until now. MFs was utilized to produce DMPC:DSPE-PEG:Chol liposomes encapsulating curcumin for sustained and controlled release in retinal tissues. Coaxial 3D bioprinting, on the other hand, was chosen to combine CUR-LPs with hydroxyethyl cellulose (HEC) and a hybrid hydrogel composed of HA and CS enriched with free RSV, achieving a burst release of the active pharmaceutical ingredient (API) and prompt

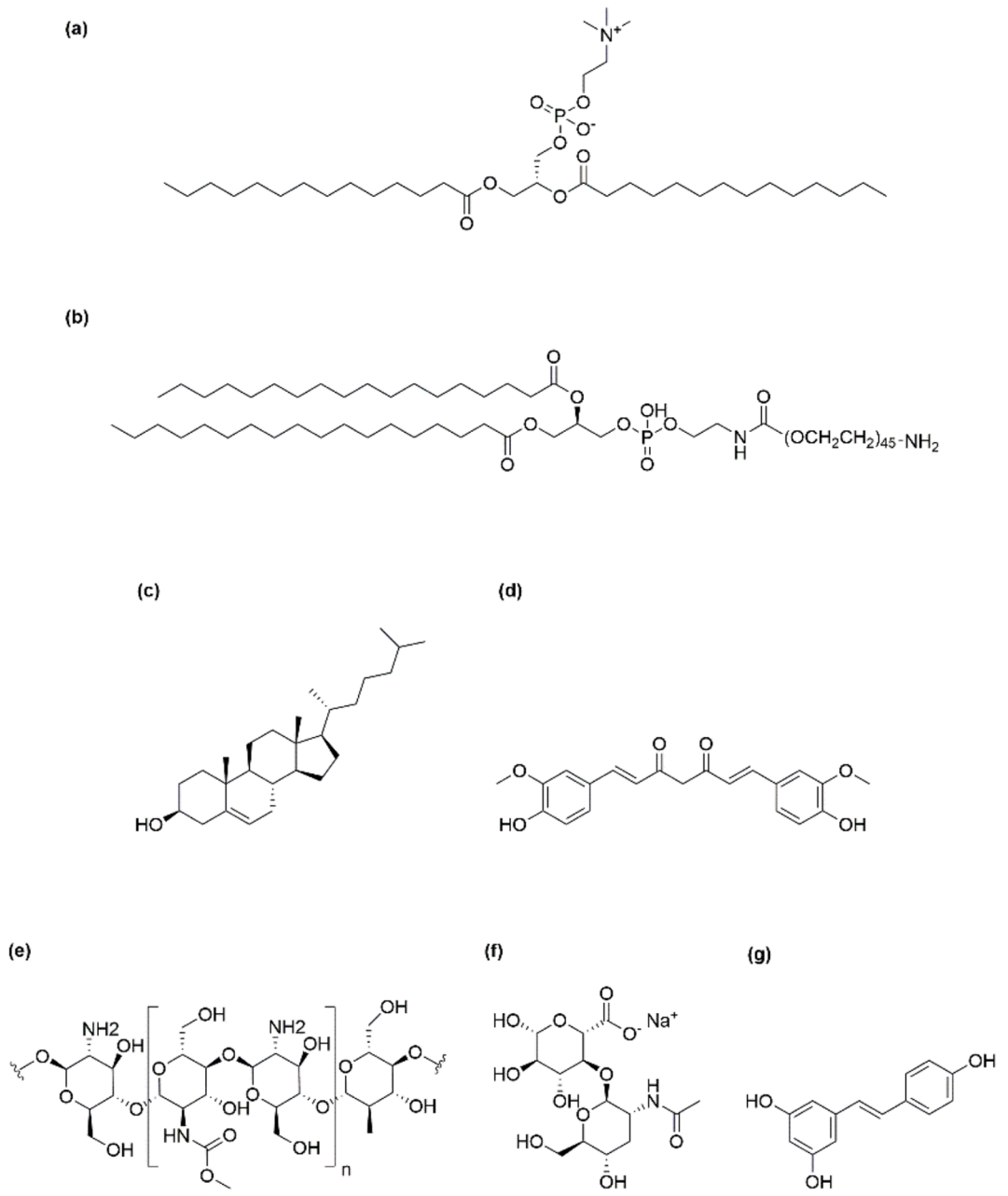

Fig. 1. The chemical structure of: (a) 1,2-Dimyristoyl-*sn*-glycero-3-phosphocholine (DMPC), (b) 1,2-distearoyl-*sn*-glycero-3-phosphoethanolamine-N-[amino(polyethylene glycol)-2000] (ammonium salt) (DSPE-PEG2000), (c) Cholesterol, (d) Curcumin (CUR), (e) Sodium Hyaluronate from Bacteria (HA), (f) Chitosan (CS), and (g) Resveratrol (RSV).

control of the inflammatory state. The resulting scaffolds were characterized and analysed to confirm proper loading of the liposomes, efficient release of both curcumin and RSV from the implant. Ultimately, cytocompatibility *in vitro* was assessed by exposing the HS/CS hydrogel scaffold with human retinal microvascular endothelial cells (HREMCs) for 72 h in culture.

2. Materials and methods

2.1. Materials

1,2-dimyristoyl-*sn*-glycero-3-phosphocholine (DMPC) was purchased from Sigma Aldrich (Germany). Cholesterol was purchased from TCI (Japan). 1,2-distearoyl-*sn*-glycero-3-phosphoethanolamine-N-[amino(polyethylene glycol)-2000] (ammonium salt) (DSPE-PEG2000) was purchased from Lipoid GmBH (Germany). Ethanol (≥99,8 %), Methanol (≥99,9 %), acetonitrile (for HPLC, gradient grade, ≥ 99,9 %), Acetic acid (for HPLC, gradient grade, 99 %) and phosphate-buffered saline tablets (PBS, pH 7.4) were purchased from Sigma-Aldrich (Germany). Chitosan (CS) high molecular weight and hydroxyethyl-cellulose (HEC) were purchased from Sigma-Aldrich (Germany). Sodium Hyaluronate from Bacteria (HA) was purchased from TCI (Japan). CUR [hydroalcoholic extract from Curcuma Longa L., rhizome; purity 95.0 % by HPLC] and RSV [*trans*-3,4′,5-Trihydroxystilbene; hydroalcoholic extract from Polygonum cuspidatum, Siebold et Zucc., roots; purity 99.0 % by HPLC] was produced by Gielleppi SpA (Seregno, Italy) and kindly gifted by Labomar SpA (Istrana, Italy). The chemical structures can be seen in Fig. 1.

Table 1
Molar ratio and FRR of Cur-LPs formulations.

Formulation code	DMPC	DSPE-PEG	Cholesterol	FRR
LPA-C 1:1	2	1	1.5	1:1
LPA-C 3:1				3:1
LPA-C 5:1				5:1
LPB-C 1:1	4	1	2.5	1:1
LPB-C 3:1				3:1
LPB-C 5:1				5:1
LPC-C 1:1	1	1	1	1:1
LPC-C 3:1				3:1
LPC-C 5:1				5:1

2.2. Manufacturing of lipid nanoformulations

CUR-LPs were prepared using the dolomite MF system, consisting of two separate pressure chambers, mitos flow sensors (0.2–5 ml/min) and a system controller. The diamond-shaped chip used is made of *PlasCLEAR* resin from ASIGA and developed using a 3DP technology as reported in previous work from our lab (Sommonte et al., 2022). The MFs parameters followed in this study have been fine-tuned based on previous works (Ballacchino et al., 2021; Jaradat et al., 2023). Keeping the mass ratios between the phospholipids and cholesterol (2:1) different ratios between DMPC/DSPE-PEG/cholesterol, are investigated (Table 1) to optimize the best formulations for curcumin loading in terms of particle size, homogeneity, stability over the time and entrapment efficiency. According to the work of Ballacchino and co-workers, the best lipid for CUR encapsulation is DMPC, in terms of small size, homogeneity, and stability (Ballacchino et al., 2021). Phospholipids and CUR at 0.1 mg/ml (w/v) were dissolved in ethanol and sonicated for 2 min to guarantee complete solubilization. The lipid phase located in one of the two chambers, and the phosphate buffered saline, prepared at pH 6.5 to ensure better stability of CUR, is inserted in the second one as the aqueous phase. The ratio between lipids was chosen according to the best composition between the materials using for pegylated liposomes preparation described in previous works (Mare et al., 2018; Moiseev et al., 2022). Different flow rate ratios (FRR; e.g., 1:2, 1:3, 1:5 ethanol: water ratio) are investigated with the same total flow rate (TFR) of 1 ml/min. According to Jaradat et al., (2022) a TFR of 1 ml/min produced liposomes based on DMPC that were smaller and exhibited better stability (Jaradat et al., 2022). Ethanol was chosen as a solvent, as it is able to solubilize both phospholipids and CUR and is compatible with ocular administration, preferably employed at low concentrations. To ensure maximum removal of the solvent and unencapsulated curcumin, purificative dialysis was adopted for all formulations. For empty liposomal synthesis, CUR was omitted from the formulation. Lipids were combined in ratios reported in table below, as to maintain 1 mg/ml total lipids in the formulation and a 2:1 ratio of phospholipids to cholesterol. Every formulation was prepared 3 times to allow for a statistical analysis.

2.3. Characterization of lipid nanoparticles

2.3.1. Particle size, polydispersity index and ζ-potential

Liposomes were characterized by determining the average particle size, polydispersity index (PDI), and zeta (ζ) potential (ZP). The analysis was conducted using the dynamic light scattering (DLS) Nanobrook Omni™ particle sizer (Brookhaven Instruments, Holtsville, NY, USA).

Table 2
Different mixtures ratio HA/CHI.

Sample	HA	CS
M1	1	1
M2	1	2
M3	1	4
M4	1	6
M5	1	8

Each measurement was carried out in triplicate at 25 °C. 20 μL of the samples were 1:100 diluted with PBS (pH 6.5) and placed into BI-SCP plastic cuvettes. Both empty LPs and CUR-LPs were analysed. Each measurement was made in triplicate.

2.3.2. Stability studies

Stability tests were performed on the LPs and CUR-LPs for up to four weeks. The samples were split into three batches and stored at room temperature (RT) and 5 °C, to mimic storage conditions and at 37 °C to mimic body conditions after administration. Particle size, PDI, and ZP were measured every week for up to 4 weeks, as previously described in section 2.3.1.

2.3.3. Encapsulation efficiency (EE%) and in vitro release

The dialysis method was used to study the EE% of the drug into the CUR-LPs. Before analysing the samples, dialysis tubes (cellulose membrane, avg. flat width 10 mm, 0.4 in, MWCO 14.000, from Sigma Aldrich, Germany) were hydrated and sterilized using boiling water. Then, 1 mL of the CUR-LP solutions (LPA-C 3:1 and LPB-C 3:1) was loaded into the tubes and soaked in 7 mL of medium (PBS pH 6.5/ MeOH at a ratio of 70:30 ratio and Tween 80 at 0.5 % w/v) to help solubilization of CUR. After 30 min, 500 μL of the outer liquid was collected and placed in vials suitable for high-performance liquid chromatography (HPLC). Analysis was carried out in triplicate and referred to a blank. The free CUR was quantified by Ultraviolet (UV) High-Performance Liquid Chromatography (UV-HPLC, 1220 Infinity LC™, from Agilent Technologies, CA, USA) that was used to evaluate the unencapsulated CUR in each sample at 425 nm using a C18 column (250 mm × 4.6 mm, from Thermo Scientific, MA, USA). Each sample underwent an 8 min elution gradient consisting of two solvents: (A) acetonitrile (ACN), and (B) 3 % v/v acetic acid in water. A 66:34 ratio between solvent A and B was employed. The overall flow rate used was 1 mL/min with a sample injection volume of 50 μL. Results were related to a calibration curve obtained for CUR in methanol which was linear in the concentration range 0.098–50 μg/mL ($R^2 = 0.9997$) evaluating the resulting peaks. Eq. (1) was used to calculate EE%.

$$\%EE = \frac{\mu gofCURadded - \mu goffreeCUR}{\mu gofCURAdded} \times 100 \quad (1)$$

The same method was used to perform the *in vitro* release. Before the analysis Cur-LPs were purified to remove excess of CUR unencapsulated following the method above. After 30 min purified CUR-LPs were placed into dialysis tubing and placed into 7 ml of medium at 37 °C to initiate release data. 0.5 ml Aliquots were taken at 0, 0.5, 1, 2, 3, 4, 6, 8, 24, 48, 72, 168, 240, and 336 h, replacing the external media with 0.5 ml of fresh PBS at 37 ∘C after each 0.5 ml aliquot, to maintain sink conditions. CUR in each withdrawal was quantified with HPLC according to the method described above.

2.3.4. Fourier-transformed (FT-IR) Infrared spectroscopy

FT-IR was utilized to further delineate the materials existing within the formulation. Analysis was undertaken using an attenuated total reflection (ATR) module-FTIR spectrometer (Thermo fisher scientific, Nicolet IS50 FTIR with built in ATR) on materials (DMPC, DSPE-PEG, Cholesterol and CUR) and LPs and CUR-LPs solid samples obtained by centrifugation (30 min at 14,000 rpm). Samples were measured over a wave range of 4000–600 cm^{-1}, over 64 scans at a resolution of 4 cm^{-1} at an interval of 1 cm^{-1}. Any background absorption was subtracted prior to analysis.

2.4. Scaffold preparation and characterisation

2.4.1. Hydrogels and scaffold Manufacturing

For the optimization, several formulations and combinations of hydrogels were prepared and tested to obtain the most suitable

printability for coaxial 3D printing. For bulk hydrogels preparation, separate solutions of sodium hyaluronate in water 1.5 % and chitosan 3 wt% were prepared in 1 % (v/v) acetic acid solution and then mixed at different ratio (Table 2). After stirring the mixture, the precipitates were left 2 h at room temperature to form the PEC. NaCl at 0.8 M was added to the complex to promote a better sol–gel transition and formation of PEC without aggregates for salt-in behaviour (Kundu et al., 2010). RSV was added to the mixture at 1 mg/ml.

To form the inner core the hydrogel of CUR-LPs was prepared. Briefly CUR-LPs was purified by dialysis method to remove the unencapsulated CUR. The CUR-LPs formulation was made suitable for 3DP in terms of viscosity, using 3 % w/v of HEC.

2.4.1.1. Rheological analysis. Rheological properties of the hydrogel formulations (Table 2) were investigated using a rotational rheometer (HAAKE™ MARS™, Thermo Fisher Scientific, USA) with a parallel plate geometry (P35/Ti, Thermo Fisher Scientific, USA) of 35 mm diameter. According to the protocols of Moroni et al., the shear rate, frequency sweep, amplitude sweep, and three-interval thixotropy test (3ITT) were performed at 25 °C, in triplicates for each mixture (Moroni et al., 2023).

2.4.2. 3D printing

The scaffolds prepared following the computer-aided design (CAD) of Fratini et al., using the same procedure of coaxial 3D-printing (Fratini et al., 2023). The aim is to obtain a hydrogel scaffold that will be cut into smaller sizes for intravitreal surgical repositioning for personalised treatment. Printing parameters have been fine-tuned to obtain the best visual printability; 25 PSI and 75 PSI were chosen as the optimal pressure values for the hydrogel in the filament's core and shell, respectively (1 PSI=6.894 kPa). The inner core of the filament embodies CUR-LPs and HEC, while the outer shell is represented by a hybrid HA/CS hydrogel. After printing, the scaffolds were soaked for 15 min in a NaOH/EtOH solution (NaOH 1 M in EtOH 96 %) to let the cross-linking reaction occur. Scaffolds were stored at 4 °C to avoid dryness.

2.4.3. FT-IR

Chemical structures of HA, CS, HEC, RSV, CUR, and spectra of blank and CUR-LPs as well as the final dry scaffolds were analysed using the same approach as described above.

2.4.4. Morphological evaluation of hydrogel scaffold

The examination of scaffolds' dimensions, and the distribution of inner core of CUR-LPs were evaluated trough microscopical analysis performed with a Leica Microsystems EZ4W microscope on the hydrogel scaffold after printing and before cross-linking process.

2.4.5. Mechanical studies

Compression tests were performed on the cross-linked scaffolds with a MultiTest 2.5-dV™ from Mecmesin (West Sussex, UK) equipped with a 300 N load cell. Tests were conducted at a constant rate of 5 mm/min at room temperature and a total of five samples were tested. Data was collected as Force vs Displacement and then plotted as stress and strain. The Young's Modulus (YM) was determined from engineering stress/strain curves and evaluating the slope of the linear region's trend line.

2.4.6. Swelling ratio, water content and degradation

The scaffold's swelling capability and water content were evaluated over time. Dried scaffolds were weighed (m_i) and then placed into 7 mL of PBS (pH 7.4) at 37 °C. At different time points (e.g., 1, 2, 4, 8, 24, 48 and 72 h), the scaffolds taken out from the medium, excess PBS was gently removed, and then reweighed (m_s). Analysis was carried out in triplicate. To calculate the swelling ratio (SWR %) and the scaffold's water content (WC %) the Eqs. (2) and (3) were used.

$$SWR(\%) = \frac{[m(s) - m(i)]}{m(i)} \times 100 \quad (2)$$

$$WC(\%) = \frac{[m(s) - m(i)]}{m(s)} \times 100 \quad (3)$$

Mass loss (ML%) was instead used to assess the degradation rate. The dry scaffolds were weighed (mi) and then placed into 7 mL of PBS (pH 7.4) at 37 °C. At each time point (e.g., 24, 48, and 72, 168, 336 h), the scaffold was removed from the medium, let dry overnight, and reweighed (md). The percentage of mass loss was calculated using Eq. (4).

$$ML(\%) = \frac{[m(i) - m(d)]}{m(i)} \times 100 \quad (4)$$

All tests were carried out in triplicate.

2.5. Drug loading

To verify the amount of CUR and RSV loaded into the scaffold, the final crosslinked 3D printed scaffolds were dissolved into 10 mL of PBS (pH 7.4) 4 % of acetic acid and 1 % of methanol at room temperature and under mild stirring, following the procedure of Lazaridou et al. (Lazaridou et al., 2024). After the scaffold was destroyed, 500 µL sample was collected and analysed after centrifugation to remove eventual piece of undestroyed scaffold. CUR was quantified according to HPLC method described in section 2.2.4.

RSV was quantified according to a method modified by Zingale et al., (Zingale et al., 2024). Ultraviolet (UV) High-Performance Liquid Chromatography (UV-HPLC, 1220 Infinity LC™, from Agilent Technologies, CA, USA) was used to evaluate RSV in each sample at 310 nm using a C18 column (100 mm × 2.1 mm, from Thermo Scientific, MA, USA). Each sample underwent a 15 min elution gradient consisting of two solvents: (A) acetonitrile (CAN), and (B) water. A 17:83 ratio between solvent A and B was employed. The overall flow rate used was 0.300 mL/min with a sample injection volume of 5 µL. Results were related to a calibration curve obtained for RSV in 30:70 EtOH/PBS which was linear in the concentration range 2.5–30 µg/mL ($R^2 = 0.9975$) evaluating the resulting peaks. The results for drug content of each molecule in the final scaffold are reported as the weight of drug (µg) and as an average of four replicates.

2.6. In-vitro drug release

Drug release studies were performed in PBS dissolution medium (0.01 M, pH 7.4) under sink conditions at 37.0 ± 0.5 °C. Static diffusion method was applied for the analysis. All scaffold formulations were immersed into vials containing 10 mL of medium and supernatant samples were withdrawn at specific time points (0.5, 1, 2 h, 4, 6 h, 24 h, 48 h, 72 h, 168 h, 240 h, and 336 h), followed by the replenishment of the withdrawn medium volume. Both drugs are quantified in each withdrawn following the same HPLC method for CUR and RSV quantification, respectively.

2.7. Cell viability assay

HRMECs (Innoprot) were seeded on fibronectin-coated culture dishes in Endothelial cell media (ECM, Innoprot), until confluency was reached. A no-scaffold culture dish was used as control, when investigating cell viability. After placing the scaffolds in the culture dishes, fresh media was added on the cells HRMECs were exposed for 72 h to the scaffold before assessing for cell viability. Cells were then washed with3 times with 1X PBS and fixed for 15 min at room temperature with 4 % formaldehyde (ThermoFisher Scientific). After fixation, cell nuclei were stained with Hoechst nuclear staining (ThermoFisher Scientific) for 15 min at RT. Cells were washed once with 1X PBS and then imaged with the Leica DMi8 inverted microscope.

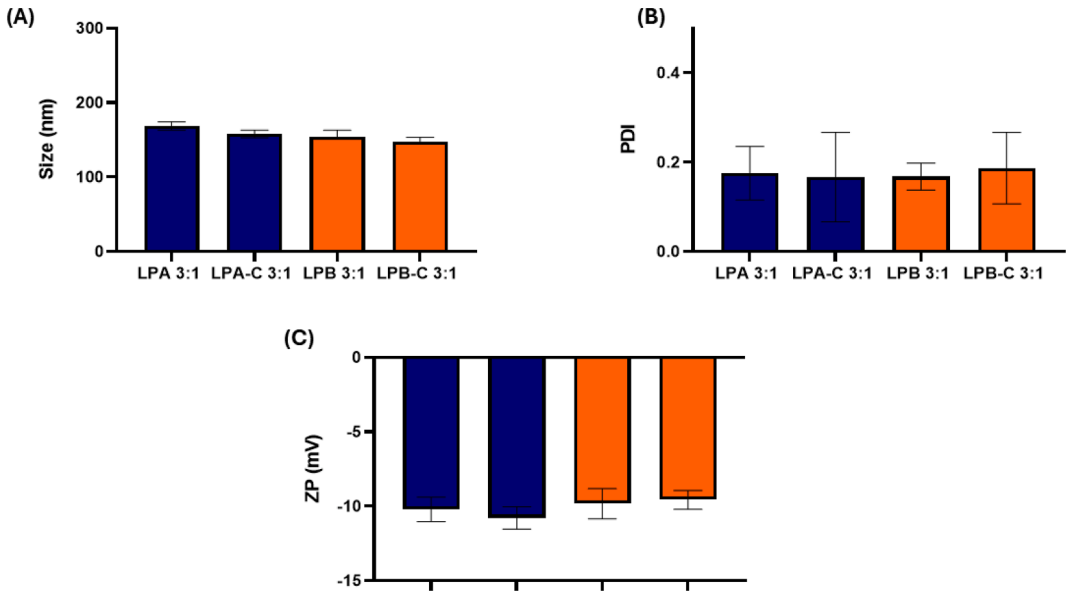

Fig. 2. Physicochemical characterization of empty LPs (LPA 3:1 and LPB 3:1) and CUR-LPs (LPA-C 3:1 and LPB-C 3:1) in terms of (A) size, (B) PDI and (C) ZP.

2.8. Statistical analysis

Experiments were conducted on several samples (n) bigger or equal to three ($n \geq 3$). All data, where possible, are expressed as mean ± standard deviation. One-way ANOVA analysis was used to determine significance using Prism 9 software, with $p \leq 0.05$ used to determine significance.

3. Results and Discussion

3.1. Liposomes

3.1.1. Physicochemical and technological characterization

The MFs approach offers the ability to produce size-controlled and homogeneously dispersed liposomal vesicles through the self-assembly of phospholipids during the process. The selection criteria for materials are based on curcumin encapsulation and achieving a small size suitable for retinal delivery.

Among all the investigated formulations reported in Table 1, only LPA 3:1 and LPB 3:1, were chosen as the ideal compositions to proceed with, based on technological parameters and reproducibility. The average size of the LPs was 168.64 ± 5.55 nm for LPA 3:1 and 154.01 ± 4.03 nm for LPB 3:1. In a normal condition neutral liposomes with a size of less than 100 nm allowed for a passage of the vitreoretinal interface. In case of DR, nanoparticles with a size until a 300 nm cross the vitreoretinal interface due to inflammation in Inner Limiting Membrane (ILM). Considering that LPA-C 3:1 and LPB-C 3:1 could cross ILM according to their size, neutrality and pegylation that better allows the vitreo-retinal passage (Tavakoli et al., 2020). They are characterized by a quite homogeneous size distribution indicated by PDI which was equal to 0.175 ± 0.060 and 0.167 ± 0.030, respectively and a slightly negative ζ-potential for the presence of DMPC and DSPE-PEG equal to

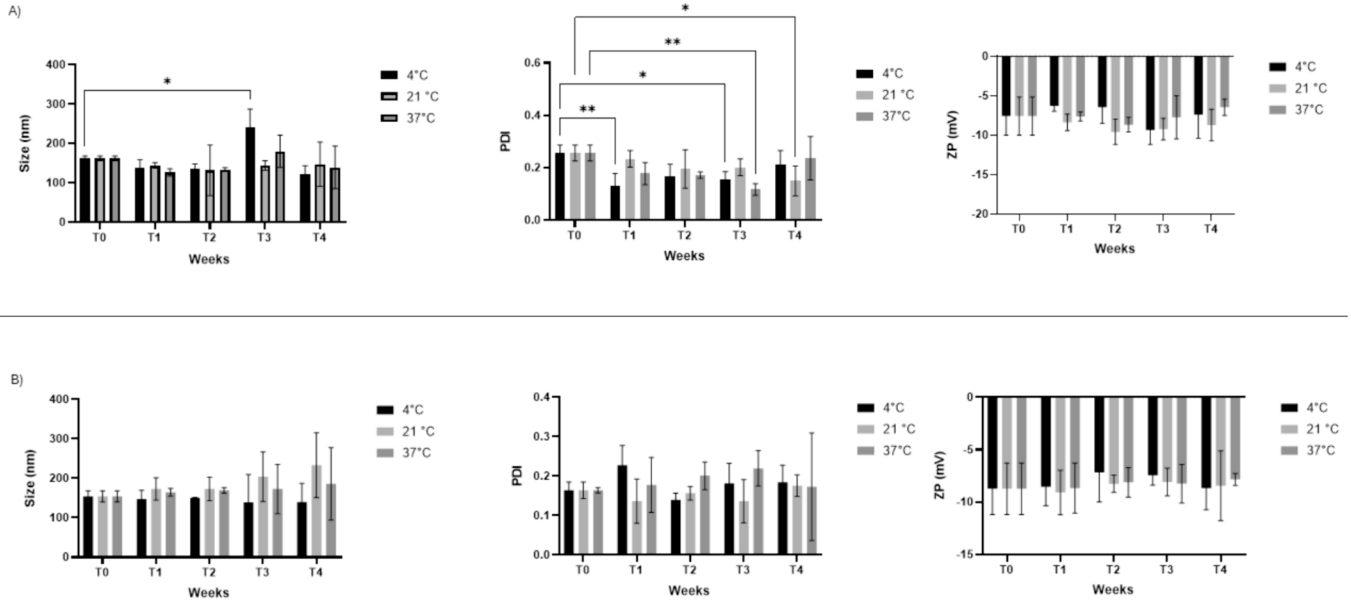

Fig. 3. Stability studies in terms of size, PDI and ZP of (A) LPA-C 3:1 and (B) LPB-C 3:1 at different storage condition (4) °C, 21 °C and 37 °C respectively assessed up to 4 weeks.

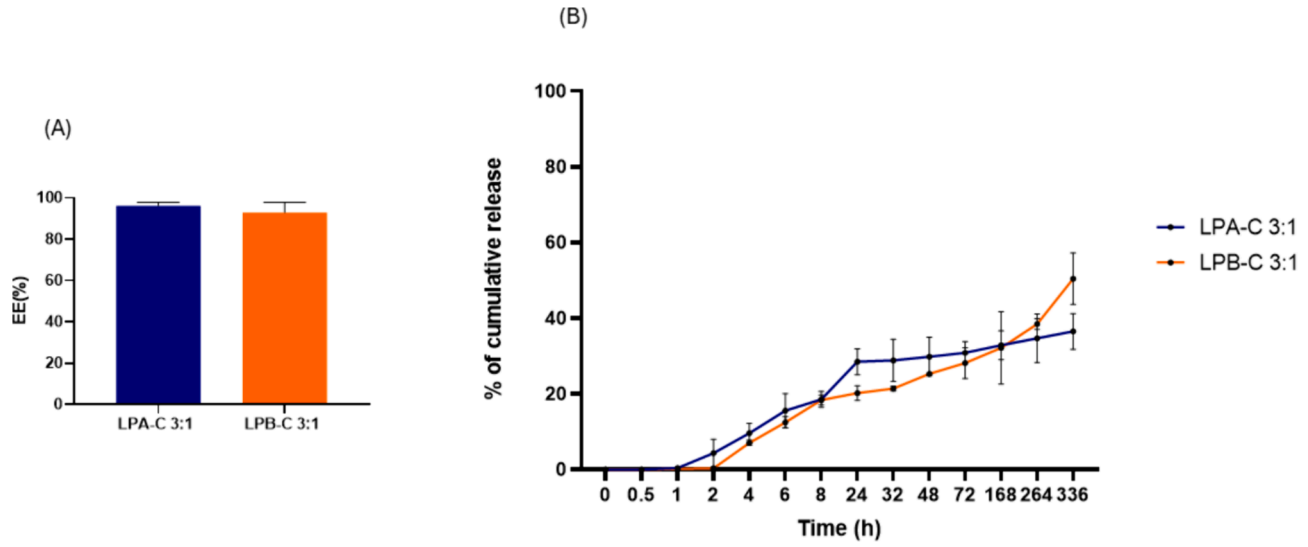

Fig. 4. (A) EE% and (B) *in vitro* release of curcumin by LPA-C 3:1 (blue curve) and LPB-C 3:1 (orange curve) in PBS (7.4, 37 °C) for 336 h. (For interpretation of the references to colour in this figure legend, the reader is referred to the web version of this article.)

−10.20 ± 0.81 mV for LPA 3:1 and −9.57 ± 1.01 mV for LPB 3:1. CUR was included in the formulation to reach final concentration above 50 μM. At a concentration above 50 μM CUR strongly reduced the proliferation of retinal cells (Hollborn et al., 2013). The inclusion of CUR inside the liposomes does not induce significant changes, with only a slight decrease in the average size. This is likely due to an interaction between the flexible lipid chains and CUR, which probably aids in forming more compact and stable particles by reducing the interlamellar spacing and causing bilayer thinning (Weaver et al., 2024). PDI remains below 0.2 and ZP remains almost unchanged (Fig. 2).

3.1.2. Stability studies

Stability studies are conducted on formulations to monitor any changes over time (Fig. 3). The evaluation should consider that formulations may be stored at different temperatures, and monitoring should also account both for the transition from storage and the temperature of ocular target site. The temperature of the eye ranges from around 30–34 °C, being lowest in the anterior part and gradually increasing towards the posterior (34 °C and 35 °C for the vitreous and retina, respectively), not exceeding 37 °C. A stability test conducted at 37 °C ensures that the formulation's behaviour under vitreous temperature conditions is adequately assessed.

The formulations tested under different conditions are stable. Visually, no macroscopic instability phenomena are observed. After 4 weeks, there is a slight increase in the size of LPA-C 3:1, which is more significant for storage at 21 °C than at 4 °C. Pegylated liposomes tend to be more stable due to the hydrophilicity of PEG, which forms a surface corona through covalent bonds, creating a hydrophilic layer that prevents aggregation (Jaradat et al., 2023; Weaver et al., 2024). The formulation does not exceed the 500-nanometer threshold, which is crucial since the barrier meshwork between the vitreous humor and retina is of this size. For better delivery, smaller sizes are generally desirable (Tavakoli et al., 2020). The LPB-C 3:1 formulation shows good stability until the end of the tested period. After 4 weeks, there is a significant size increase at 21 °C and 37 °C. In terms of PDI and ZP, the LPA-C 3:1 formulation is more stable, as no significant changes are reported. Both formulations demonstrate good homogeneity with a PDI of less than 0.3. However, there is a decrease in ZP after two weeks for the LPB-C 3:1 formulation, shifting from around −10 mV to approximately −20 mV. This increases in the negative value, compared to the value observed at time 0, could be due to CUR being released from the liposomes into the medium. The zeta potential of curcumin alone is −20.18 ± 0.46 mV, which supports this observation. This trend is not seen in the blank formulation (Figure S1, Supplementary materials), confirming that the increase in anionic charge is likely due to the release of the active ingredient. The CUR release could also lead to precipitation as crystals, resulting in aggregates that increase the average particle size after 4 weeks.

3.1.3. EE% and in vitro release

Evaluation of encapsulation efficiency (EE%) is crucial to understand the capacity of liposomes to retain a certain amount of drug, ensuring proper concentration for treatment and minimizing drug wastage during preparation. The calculated EE% was 96.24 ± 1.59 % and 92.93 ± 4.88 % for LPA-C 3:1 and LPB-C 3:1, respectively, as shown in Fig. 4A. This high embedding efficiency aligns with previous studies using the same microfluidic preparation method (Ballacchino et al., 2021). The high efficiency within the liposomes is attributed to their effective retention of CUR, likely due to its interaction with the phospholipids, particularly DMPC (Jaradat et al., 2023; Sahu and Mishra, 2021). Short-chain phospholipids and the amount of cholesterol enhance the entrapment of a hydrophobic drug by increasing the membrane's hydrophobicity (Jaradat et al., 2022). Additionally, positioning lipophilic drugs in the core allows for greater encapsulation (~90 %) due to the larger space of the liposomal core compared to the hydrophilic matrix available for hydrophilic drug accommodation (Jalili and Saeedi, 2016).

Assessing drug release under conditions that mimic physiological conditions is crucial for predicting in vivo performance and drug stability in a simulated environment over time. Many factors influence liposome release, such as cholesterol content, temperature, and pH of the medium, salt concentration, the nature of the drug, and membrane composition (Tamam et al., 2019).

In the first 24 h, less than 30 % of the drug was released from LPA-C 3:1, and around 20 % was released from LPB-C 3:1 (Fig. 4B). The initial burst release at 6 h, with a release of around 15 % and 12 % respectively, is related to the concentration difference between the external medium and the liposome core containing CUR. This difference allows a controlled release of CUR in the following hours. This release is likely facilitated by the PEG corona covalently linked to the liposome surface, which delays the release of CUR. The release is controlled for 2 weeks (336 h), with 36 % of the total CUR content released from LPA-C 3:1 and around 50 % from LPB-C 3:1. The larger amount of CUR released by LPB-C 3:1 after 168 h is consistent with the stability study results, where the zeta potential decreases after 2 weeks of storage, further confirming the

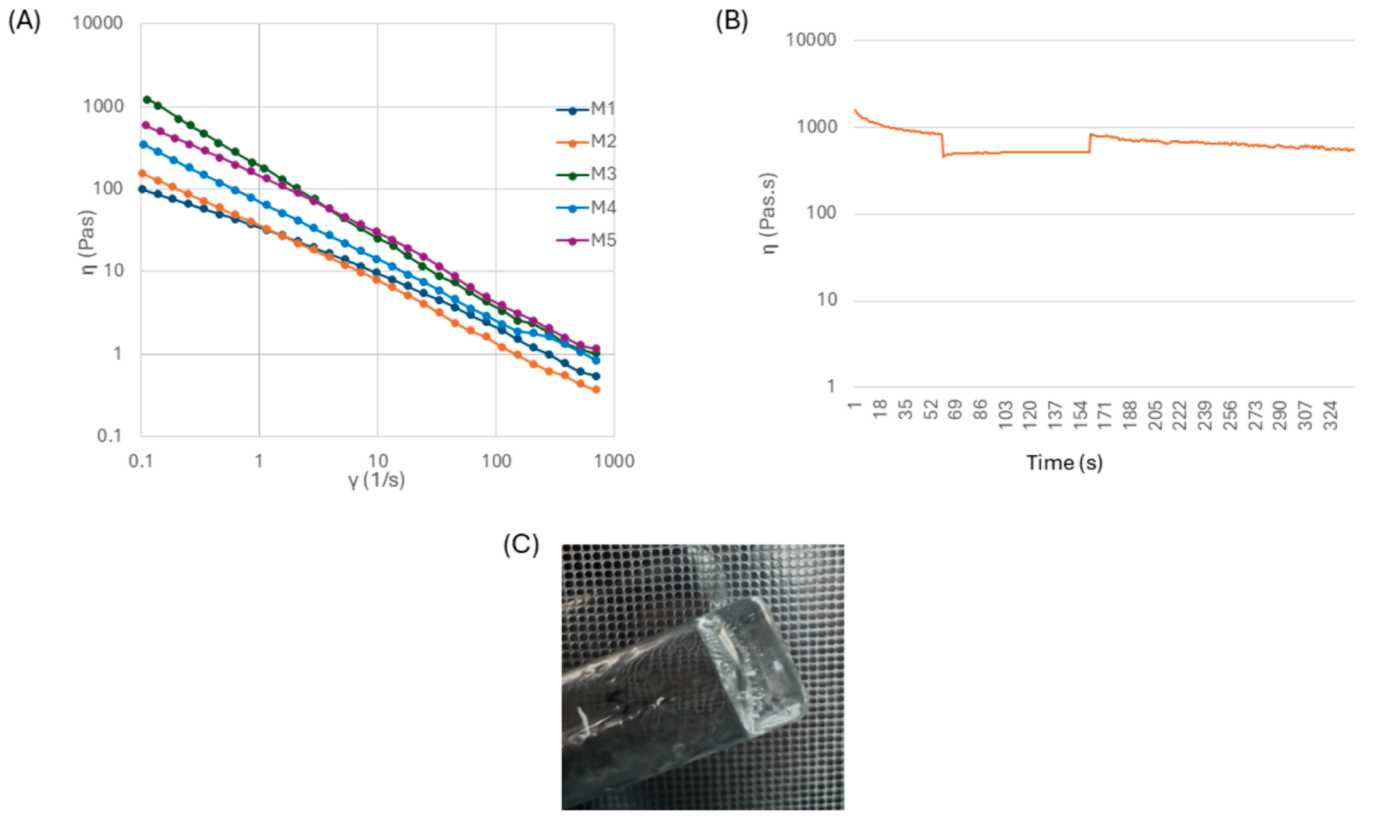

Fig. 5. Rheological behaviour in terms of (A) M1-M5 viscosity subjected to increasing shear stress (B) 3ITT results of M5 and (C) macroscopic evaluation of M5 mixture after flipping.

release of CUR. This percentage could be further prolonged due to the viscous nature of the vitreous humor, which slows down the dissolution of liposomes.

Long-term release is important since DR is a chronic disease requiring long-term therapies. Rapid release increases the risk of side effects, reduces patient compliance due to the need for repeated administration, and increases healthcare costs. Liposomes act as a long-release system for at least 14 days, as reported by other studies (Fratini et al., 2023). As expected, a 2:1 ratio of phospholipids to cholesterol in liposomes helps achieve controlled drug release over time, as previously investigated by Briuglia et al. (Briuglia et al., 2015). The concentration of CUR released in the last 2 weeks by both formulations is sufficient for the therapeutic effect of the Sirt1 protein agonist, so both formulations should be continued as suitable for the purpose of the work.

3.1.4. FT-IR analysis

The characterization of the liposome formulations using FTIR was conducted to perform a comparative study between the phospholipids and formulated liposomes, both loaded (LPA-C 3:1 and LPB-C 3:1) and unloaded (LPA 3:1 and LPB 3:1) (supplementary materials; Figures S2 and S3, respectively). The main peaks identified in the analysis are consistent with those reported in the literature and are represented in Table S1 of the supplementary materials.

As shown in supplementary materials (Figures S2 and S3), the spectra of blank liposomes are superimposable with those of CUR-liposomes. All liposome preparations display similar spectra with characteristic peaks between 2900 cm^{-1} and 2800 cm^{-1}, indicating –CH3 and –CH2 stretching vibrations, respectively, suggestive of the acyl chain flexibility of the lipids used (Briuglia et al., 2015). The peak of CUR around 3500 cm^{-1} related to phenolic O–H (Ismail et al., 2014) disappeared in the spectra of CUR-LPs indicating probably a good encapsulation of the molecule inside the LPs (Zingale et al., 2022). After encapsulation with CUR, a shift was observed in the symmetrical C–H stretching region with a reduction in peak intensity in the C–H stretching region and disappearance of a peak at 3016 cm^{-1}. Also, slight changes in the region of phosphate group (1300–900 cm^{-1}) are evident. The possible interaction of CUR with phospholipids means that the polar head groups of lipid molecules are more separated from each other and have greater freedom of movement (Duda et al., 2020). All experimental wavenumber for each FT-IR spectra is reported in Table S1 in SI.

3.2. Hydrogel scaffolds

3.2.1. Hydrogel mixtures evaluation

The primary aim is to create a hydrogel scaffold composed of highly biocompatible and biodegradable materials. Using HA and CS allows for a soft, deformable system suitable for intravitreal repositioning. HA, a component of the vitreous humour, is rarely used alone and is often functionalized (e.g., as methacrylate) to enhance its mechanical properties (Fan et al., 2020). Its high compatibility and transparency make it an ideal candidate for intravitreal scaffolds. To address its poor mechanical properties, we chose to form a PEC with CS. CS, a natural material, is known for its biodegradability and adhesive properties, which help prevent the implant from migrating toward the anterior chamber. This advantage is typical of many implants. Forming the bioink from chitosan and HA without prior chemical modifications is challenging. As reported by Mais-Fernandez et al., the printability of the formed hydrogel is a significant challenge (Maiz-Fernández et al., 2021). The pH, salt concentration, and molecular weight of the materials can influence the stability and printability of the bioink (Khoonkari et al., 2023). To promote electrostatic interactions between the carboxylate groups (–COO-) of HA and the amine groups (–NH3 +) of chitosan, the pH was adjusted to acidic during preparation to maximize the ionization of both polyelectrolytes. Adding NaCl was used to enhance the formation of the complex by increasing salting-in phenomena and improving material interactions (Khoonkari et al., 2023). FT-IR spectra, reported in

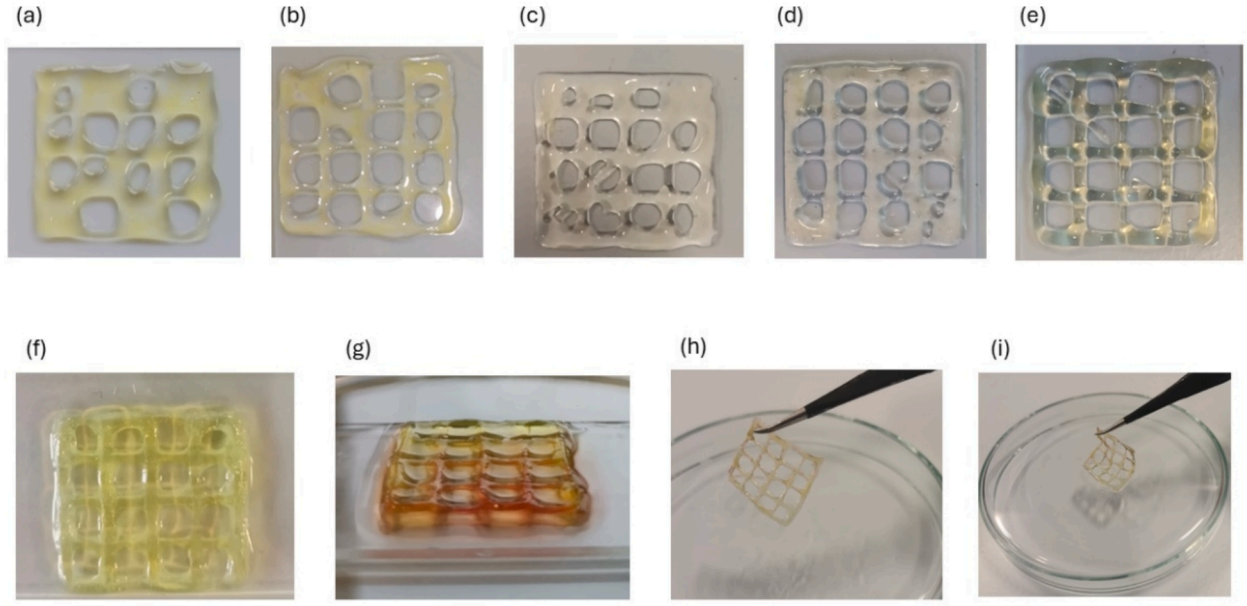

Fig. 6. Printed scaffold with mixtures a) M1 1:1 (HA/CS); b) M2 1:2 (HA/CS); c) M3 1:4 (HA/CS); d) M4 1:6 (HA/CS); e) M5 1:8 (HA/CS) and CUR-LPS+3% of HEC. Cross-linked scaffold after cross-linking (f) up view and (g) lateral view. Dried scaffold after cross-linking (h) and (i).

the supplementary materials (FigureS4), confirmed the formation of a PEC between chitosan and hyaluronic acid due to a slight shift in the amine bond bands (3300 cm^{-1}), indicating interactions between the polysaccharides (Barroso et al., 2019). This trend was not observed under different conditions, such as without salt addition, confirming that specific conditions are crucial for complexation.

Rheological studies were conducted for each mixture presented in Table 2 before printing. As shown in Fig. 5A, all mixtures exhibited shear-thinning behaviour, characterized by a decrease in viscosity as the shear rate increased. Mixtures M3 and M5 presented high viscosity, with M5 demonstrating the highest linearity, showing a very linear curve with increasing stress and maintaining higher viscosity than others. The increasing amount of chitosan in M5 resulted in higher viscosity due to chitosan's gelling properties and provided a good shear-thinning effect, a fundamental requirement for achieving good printing performance and avoiding the collapse of the printed scaffold (Cho et al., 2006).

All mixtures exhibited a similar trend in which G' was higher than G'' (supplementary materials figure S5). Both values tended to increase as the concentration of CS in the mixtures increased (Cho et al., 2006). G' represents elastic behaviour, while G'' represents viscous behaviour. Except for M1, which reported a G'' value higher than G', likely due to inadequate interaction between materials, the other mixtures showed a G' curve consistently higher and visually distinct from the G'' curve. Gel and elastic behaviour predominated in all mixtures, indicating strong gel formation optimal for preventing scaffold collapse after printing. It is interesting to note that rheological studies related to vitreous humor also reported a viscoelastic behaviour, with G' higher than G'' (Cho et al., 2006).

The 3ITT test provided essential information on the recovery rate after extrusion, which is associated with mould fidelity. Therefore, viscosity was analysed over time with different shear values applied to simulate different stages of the printing process. Specifically, the recovery capacity was determined at three intervals with low, high, and low shear values, simulating respectively: the resting phase before the printing process, extrusion, and the period immediately after the printing process. Although all blends exhibited very good recovery values, the M5 blend (Fig. 5B) demonstrated, in line with the previous rheological results, excellent formation of a transparent and viscous gel suitable for high-quality printing (see Fig. 5C). Moreover, for intravitreal implants, transparent materials may be preferred over opaque materials (García-Estrada et al., 2021).

3.2.2. 3D printed hydrogel scaffolds

Different mixtures with different HA:CS ratios (1:1, 1:2, 1:4, 1:6 and 1:8) are tried and printed as shown in Fig. 6(a–e). Implants were designed by Tinkercad and manufactured by an extrusion method by coaxial 3DP. The only mixture that retained its structure after being printed without collapsing was the HA:CS with 1:8 ratio.

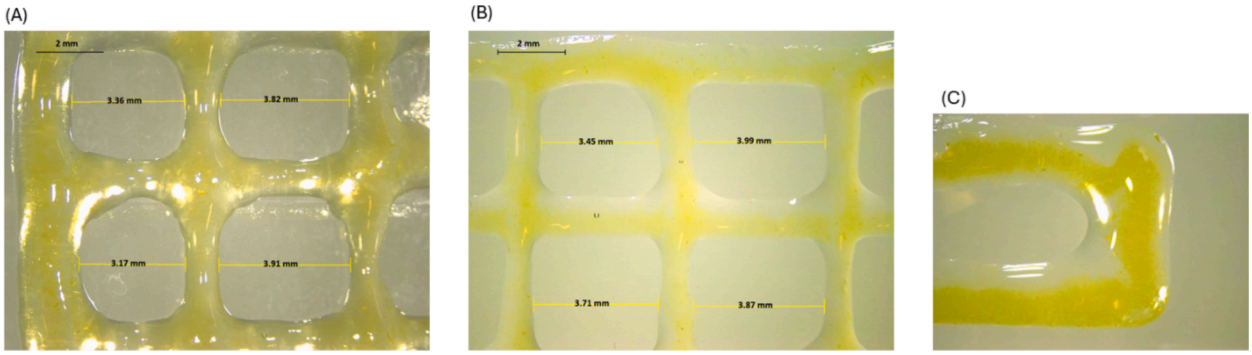

Fig. 7. Inside of the scaffold after all printing (A), after first layer (B) and (C)filament inside of CUR-LPs.

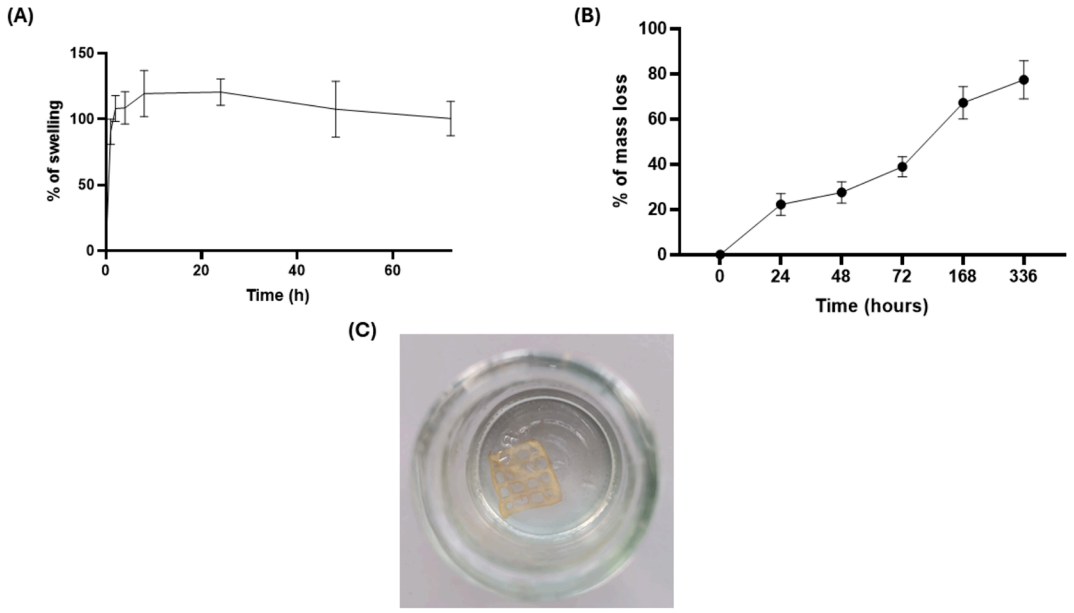

Fig. 8. A) Scaffold's swelling (%) through time; B) Scaffold's mass loss (%) and (C) visual observation of scaffold in PBS after 336 h.

RSV was embedded in mixture at a concentration of 50 μM. RSV at concentrations of 50 μM was protective in retinal cells against cell proliferation, migration, and fibronectin synthesis, typical of advanced stages of diabetic retinopathy through the regulation of a Sirt1-related pathway (Cao et al., 2020; Ishikawa et al., 2015).

The condition (printing pressure: 25.1 PSI inner core and 74.6 PSI outer core at 25 °C) was selected as optimal printing condition to obtain scaffold as in Fig. 7e and applied in later experiments as a better printing result can be enabled under this condition.

Once the scaffold is obtained, it needs to be cross-linked to obtain a solid structure that can be managed for subsequent studies. One of the most used solutions of multivalent ions of opposite charge, $CaCl_2$ is the one most used to promote crosslinking of HA with polymers by covalent bonds, such as CS in our case (Khunmanee et al., 2017). The trial did not yield any results probably due to the lower proportion of HA in the mixture. Glutaraldehyde acting as a cross-linker for CS made it possible to obtain a more structured scaffold. To avoid using glutaraldehyde, a NaOH/EtOH solution was tried for placement in ocular tissues, with very good results. Following the work of Lazaridou et al., this solution helps the cross-linking of structures with CS, and it is an optimal alternative to conventional use of dialdehydes which presents cytotoxicity and biocompatibility issues (Lazaridou et al., 2024). Only in the mixture with a ratio of 1:8 HA/CS was it possible to achieve cross linking of the layers (Fig. 6f) without affecting the inner liposome core and to avoid a degradation of the curcumin liposomes (from yellow to red colour change of curcumin that degrades in basic environments) Fig. 6g. The hydrogel obtained from the HA/CS 1:8 polyelectrolyte complex provides protection of the inner layers of the scaffold. The efficiency of the crosslinking can be observed in Fig. 6h and 6i in which the scaffold is detached from the petri dish where it was printed and a precise (Fig. 6h) and deformable (Fig. 6i) scaffold is evident. At alkaline pH values amino groups are deprotonated, which induces CS polymer precipitation and formation of easily manipulated gels that can be used as matrix material to build tridimensional scaffolds to be implanted in vivo (Martín-López et al., 2012). The use of the light microscope made it possible to detect the presence of the inner filament consisting of CUR-LPs as shown in Fig. 7. Staining of the liposomes was not necessary as CUR is a visibly detectable molecule and allowed sharp images of the inner filament to be obtained. It is homogeneously distributed in all layers within the HA/CS hydrogel matrix after the printing process, which did not affect the liposome structure.

Filament homogeneity and uniformity are important parameters that need to be considered. The pore size of the scaffold has an average diameter of 3.66 mm ± 0.28 mm, based on eight samples tested. The theoretical value is 4 mm. The actual size is 91.5 % of the theoretical value, representing a good result for a multilayer structure composed of hydrogels, which are exposed to swelling and deformability during 3D printing process due to their nature.

3.2.3. *FT-IR analysis of the 3DP scaffolds*

FT-IR analysis is important here to define the formation of the polyelectrolyte complex in the HA-CS mixture, which was reported in supplementary materials (Figure S6). In this section, an analysis made on three different locations of the scaffold under investigation will be shown to assess the homogeneous distribution of the materials. As reported also in the table S2 in supplementary materials, the characteristic peaks of chitosan appear at 1648.17 cm^{-1} and around 1500 cm^{-1} (small peaks) corresponding to amide I and amide II bands, respectively. It also shows the twisting of –CH2 group at 1374.24 cm^{-1} and C-N stretching at 1311.28 cm^{-1}. The amide I and amide II bands of HA are observed at 3279 $cm^{-}1$ and 1604.19 cm^{-1} respectively, the asymmetric and symmetric stretching of carboxylate group appears at 1604.19 cm^{-1} 1405.35 as well as C-N stretching at 1375.32 cm^{-1}. There is a shift between 3289.49 (CS) corresponding to stretching vibration of free amine (–NH2) and hydroxyl (–OH) groups and the same for the peak at 3272.69 cm^{-1} of HA when they are in mixtures. There is an overlapping of the peaks and a shift when the mixture is present and even more evident in the scaffold under analysis. The interaction means that there is a single peak around 3342 cm^{-1} by interaction of the two molecules forming the PEC (Martín-López et al., 2012). The same is reported for the peak at 1648.17 cm^{-1} corresponds to Amide I (RC=O-NH2) proper to CS appeared slightly displaced in the mixtures which were presumably related to the formation of weak electrostatic bonds with HA. The observed overlap of CS and HA bands suggests the involvement of both polysaccharides in HA/CS systems. The interaction found in the mixture (Figure 2SI) is also evident in the spectra of the final scaffold where three points are randomly analysed and in which the maintenance of interaction may be attributed to increased interpenetration during the layer-by-layer deposition after printing. In the fingerprint region (900–1500 cm^{-1}) the mixtures exhibited bands at a lower wave number compared to the CS or HA individual molecules, indicative of the weak electrostatic bond formation (Barroso et al., 2019).

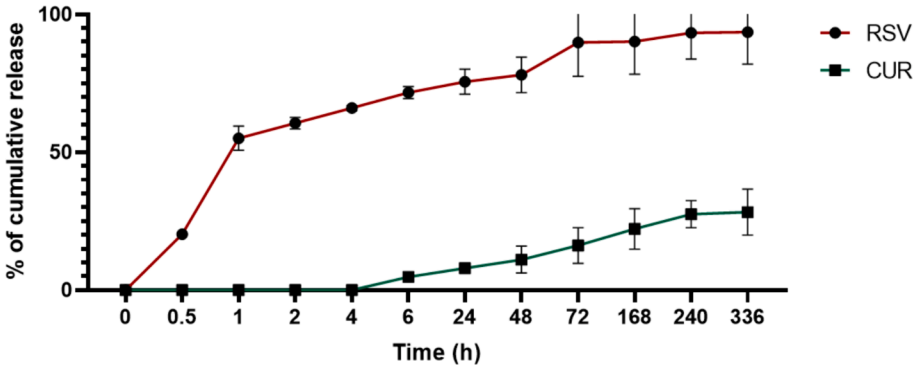

Fig. 9. Cumulative drug release trend line of CUR from the inner core (green line) and RSV from the outer shell (red line) of the printed scaffold. (For interpretation of the references to colour in this figure legend, the reader is referred to the web version of this article.)

The RSV peaks are not visible as they fall within the peak of the mixture in particular the peak the distinctive peak at 3177.83 cm^{-1}, characteristic of phenolic compounds and at 1604.75 cm^{-1} typical of C–C aromatic double bond stretching. Concluding, the FTIR data (supplementary material; Figure S6) shows three completely overlapping spectra indicating that all materials are homogeneously distributed within the scaffold. The absence of this peak, as observed for CUR-LPs, indicates that RSV and CUR are well incorporated into the mixture. The peaks of the zone of analysis in the scaffold are reported in Table S2 together with a mean peak of raw materials.

3.2.4. Swelling ratio and degradation

The dry scaffold exhibited a notable swelling capability immediately after 1 h of being soaked in 7 mL of PBS at 37 °C, reaching a maximum peak of 120.58 ± 10.03 % of swelling after 24 h (Fig. 8A). The total water content was assessed to be 54.60 ± 2.11 %. It is crucial that the implant does not undergo excessive swelling, as it could pose risks such as increased pressure in the vitreous chamber, inflammation, fragmentation with migration, and discomfort (Roh et al., 2018).

However, hyaluronic acid-based hydrogel resulted in a soft and safe material for intravitreal implantation, with biodegradation depending on material modifications. After 24 h, a plateau in the swelling trend is observable until a trend reversal occurs due to the degradation process taking place. We anticipated these results since no modifications were made to HA (Avitabile et al., 2001). This can be confirmed by evaluating the scaffold's mass loss over time (see Fig. 8B). The scaffold becomes thicker but maintains its structure until the final analysis, as reported in Fig. 8C.

It's interesting to observe, from video S1 provided, that the scaffold, although folding upon placement in an aqueous environment such as could be the vitreous humor of the eye, maintains its original shape. This observation is very interesting because, in the scenario of minor surgery requiring folding and positioning of the scaffold at the target site, it would regain its original shape once placed there.

3.2.5. Mechanical evaluation of the scaffolds

The 3D-printed scaffolds underwent compression testing to investigate their mechanical properties, specifically their Young's Modulus (E), which was determined as the slope of the linear segment of the stress–strain curve and was found to be 1.12 ± 0.087 MPa. CS typically exhibits a Young's Modulus ranging from 7.06 MPa to 9.5 MPa depending on its molecular weight (Bentley et al., 2022; Le et al., 2012). However, studies have shown that when combined with other materials such as HA, this value tends to decrease, rendering the scaffold stiffer and more elastic. A low Young's Modulus indicates that the scaffold possesses elastic properties, undergoing significant (elastic) deformation under relatively low loads. The scaffold demonstrates high flexibility, as depicted in Fig. 8. The selected printing mixture yielded hydrogels with flexible drug delivery properties, crucial for optimal implant repositioning during intravitreal surgery. Nonetheless, it is essential for the mechanical strength to remain intact to facilitate implant placement and drug delivery without significant bending or breakage of the implant system, thereby ensuring the scaffold's elastic behaviour allows it to withstand pressure during implantation without deformation (McAvoy et al., 2018).

3.2.6. Drug loading and in vitro release

The *in vitro* release test is essential for evaluating whether the amount of drug released is adequate to produce a therapeutic effect. Obtaining results directly comparable to in vivo tests, especially for implants designed for posterior eye delivery, presents challenges, but efforts are made to closely simulate the physiological environment (Adrianto et al., 2022). In our case, with a dual-loaded drug exhibiting different localizations, it is crucial to assess the actual release of the two molecules over time. A static diffusion test was adopted to best analyze both drugs from the scaffold, considering the degradation nature of the scaffold itself, and PBS at a pH of 7.4 was used as a medium to better simulate the conditions of the vitreous humor (Adrianto et al., 2022). Fig. 9 reported the release pattern observed for both molecules from the scaffold. The amount of RSV found within the scaffold in the hydrogel matrix of HA/CS is 190.30 ± 3.01 μg, and that of CUR is 3.40 ± 1.07 μg. The release of RSV from the scaffold commences at 30 min, with approximately 20 % released, reaching a maximum release after two weeks of 93 %. This aligns with the swelling activity observed at 1 h, suggesting that the rapid release of RSV may be related to this phenomenon. The quantity of RSV released within the first 30 min is already sufficient to activate Sirt1. Cao et al., (2020) reported that concentrations as low as 30 μM, administered via intravitreal injection, are effective in restoring the activity of Sirt1 in retinal ganglion cells (Cao et al., 2020). In contrast, the release of CUR is slow, involving an initial release from the liposomes followed by subsequent release from the hydrogel as it degrades through swelling or flaking. CUR release from the scaffold initiates at 24 h, indicating delayed drug release, with only 4.78 % released before 24 h. The release gradually increases to 28.28 % by 336 h. Additionally, the amount of CUR released starting from 48 h (11 % cumulative release) is sufficient to activate Sirt1. A concentration of 1 μM CUR is adequate to enhance Sirt1 regulation, and the concentration released by our scaffold surpasses this requirement (Yang et al., 2013). The dual and differential localization of the two drugs enables an initial release of RSV, which, as a potent Sirt1 agonist, exhibits anti-inflammatory action. As CUR is released, it contributes to antioxidant effects and anti-VEGF activity. Slow release is significant in ocular degenerative diseases as it obviates the need for repeated and invasive administration to the posterior tissues. Hydrogel scaffolds offer localized controlled drug release over an extended period, addressing the therapeutic needs effectively.

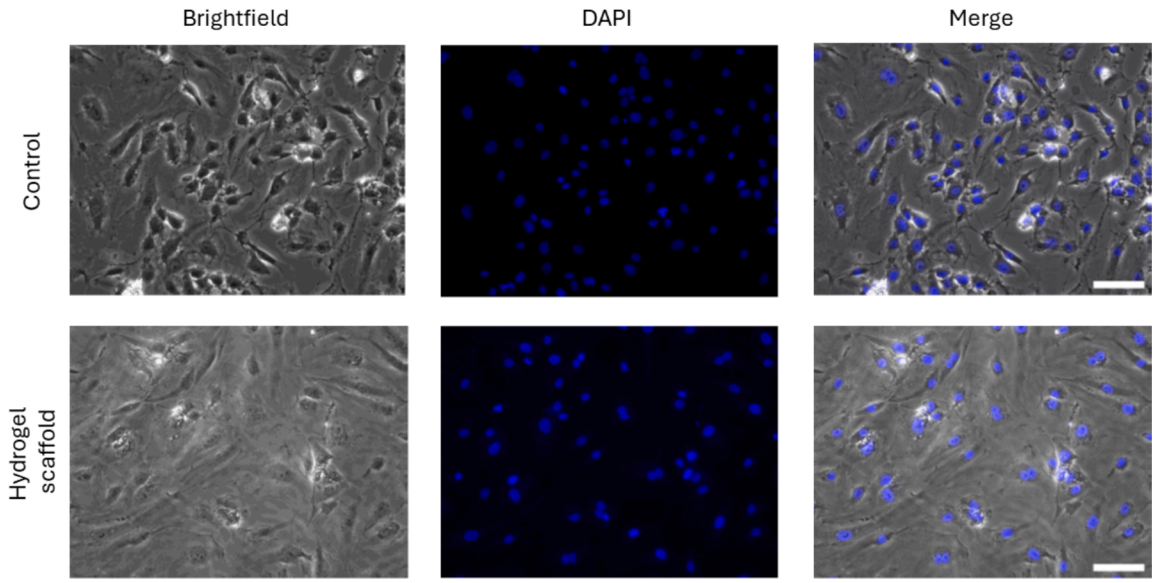

Fig. 10. Representative brightfield images of HRMECs *in vitro* to assess cell viability of untreated cells (top row) and exposed to hydrogel scaffold for 72 h (bottom row). DAPI (blue) was used to stain cell nuclei. Scale bar: 100 μm. (For interpretation of the references to colour in this figure legend, the reader is referred to the web version of this article.)

3.2.7. Hydrogel scaffold biocompatibility in vitro

One of the aims of the work is to develop a highly biocompatible hydrogel scaffold. Natural or endogenous materials such as HA, a major constituent of the vitreous humor, were used for this purpose. The cytocompatibility of the scaffold was tested on human retinal endothelial microvascular cells (HRMECs). Cells exposed for 72 h showed no signs of stress after exposure with the HA/CS scaffold, proving the biocompatibility of the system (Fig. 10). The loaded system was not compatible under these conditions. From our release studies previously described, loaded scaffolds release an RSV concentration of approximately 300 μM after 72 h. A concentration of RSV above 150 μM is not tolerated by cell *in vitro*, and it has been reported to increase the expression of the proapoptotic effectors Bak and Bax, inducing cell death (Nakagawa et al., 2001). Further studies will be conducted to investigate the optimal concentration of drug within the system, to improve the compatibility of RSV-loaded hydrogel scaffolds.

4. Conclusions

The successful integration of liposomes (LPs) and hydrogels in the creation of 3D-printed (3DP) hydrogel scaffolds enables the delivery of different molecules, such as RSV and CUR, which are differently localized within the system, ensuring bulk and sustained release. The study demonstrates that MFs and 3D bioprinting can be effectively combined to produce versatile carriers capable of accommodating various APIs, thereby achieving multiple release profiles. The resulting hydrogel scaffold exhibits features suitable for intravitreal implantation and the treatment of diabetic retinopathy. With their softness and high biocompatibility, hydrogels are optimal candidates for ophthalmic applications, and hydrogel-based nanosystems with biocompatible and bioadhesive properties show promise in this preclinical technological study. While the primary aim of this study was to demonstrate the synergy between these two methodologies, additional cellular research is required to confirm the scaffold's effectiveness in a diabetic retinopathy model. This represents an important step in exploring different platforms such as implantable devices and investigating the potential of personalized medicine, facilitated by 3DP approaches. Developing and improving these treatments is crucial for creating effective dressings that deliver molecules effectively to the posterior segment of the eye, reducing the need for repeated administrations in chronic diseases, and enhancing patient compliance among affected individuals.

Funding

E. Z. is beneficiary of a grant from the Ph.D. course in Neuroscience, XXXVII cycle, University of Catania.

CRediT authorship contribution statement

Elide Zingale: Writing – review & editing, Writing – original draft, Validation, Methodology, Formal analysis, Data curation, Conceptualization. **Edward Weaver:** Writing – review & editing, Writing – original draft, Methodology, Investigation, Formal analysis, Data curation, Conceptualization. **Pietro Maria Bertelli:** Writing – review & editing, Writing – original draft, Methodology, Investigation, Data curation. **Imre Lengyel:** Writing – review & editing, Supervision, Resources, Methodology. **Rosario Pignatello:** Writing – review & editing, Supervision, Resources. **Dimitrios A. Lamprou:** Writing – review & editing, Validation, Supervision, Resources, Project administration, Methodology, Funding acquisition, Formal analysis, Conceptualization.

Declaration of competing interest

The authors declare that they have no known competing financial interests or personal relationships that could have appeared to influence the work reported in this paper.

Data availability

Data will be made available on request.

Appendix A. Supplementary material

Supplementary material to this article can be found online at https://doi.org/10.1016/j.ijpharm.2024.124700.

References

Abou Taha, A., Dinesen, S., Vergmann, A.S., Grauslund, J., 2024. Present and future screening programs for diabetic retinopathy: a narrative review. Int. J. Retina Vitreous. 10 (1), 14. https://doi.org/10.1186/s40942-024-00534-8.

Adrianto, M.F., Annuryanti, F., Wilson, C.G., Sheshala, R., Thakur, R.R.S., 2022. In vitro dissolution testing models of ocular implants for posterior segment drug delivery. Drug Deliv. Trans. Res. 12 (6), 1355–1375. https://doi.org/10.1007/s13346-021-01043-z.

Amato, G., Grimaudo, M.A., Alvarez-Lorenzo, C., Concheiro, A., Carbone, C., Bonaccorso, A., Musumeci, T., 2020. Hyaluronan/poly-L-lysine/Berberine Nanogels for impaired wound healing. Pharmaceutics 13 (1), 34. https://doi.org/10.3390/pharmaceutics13010034.

Avitabile, T., Marano, F., Castiglione, F., Bucolo, C., Cro, M., Ambrosio, L., Reibaldi, A., 2001. Biocompatibility and biodegradation of intravitreal hyaluronan implants in rabbits. Biomaterials 22 (3), 195–200. https://doi.org/10.1016/S0142-9612(00)00169-1.

Ballacchino, G., Weaver, E., Mathew, E., Dorati, R., Genta, I., Conti, B., Lamprou, D.A., 2021. Manufacturing of 3D-printed microfluidic devices for the synthesis of drug-loaded liposomal formulations. Int. J. Mol. Sci. 22 (15), 8064. https://doi.org/10.3390/ijms22158064.

Barroso, N., Guaresti, O., Pérez-Álvarez, L., Ruiz-Rubio, L., Gabilondo, N., Vilas-Vilela, J. L., 2019. Self-healable hyaluronic acid/chitosan polyelectrolyte complex hydrogels and multilayers. Eur. Polym. J. 120, 109268 https://doi.org/10.1016/j.eurpolymj.2019.109268.

Barth, H., Crafoord, S., Andréasson, S., Ghosh, F., 2016. A cross-linked hyaluronic acid hydrogel (Healaflow®) as a novel vitreous substitute. Graefes Arch. Clin. Exp. Ophthalmol. 254, 697–703. https://doi.org/10.1007/s00417-015-3256-z.

Bentley, F.E., Passieux, R., David, L., Osorio-Madrazo, A., 2022. Pure chitosan biomedical textile fibers from mixtures of low-and high-molecular weight bidisperse polymer solutions: processing and understanding of microstructure-mechanical properties' relationship. Int. J. Mol. Sci. 23 (9), 4767. https://doi.org/10.3390/ijms23094767.

Briuglia, M.L., Rotella, C., McFarlane, A., Lamprou, D.A., 2015. Influence of cholesterol on liposome stability and on in vitro drug release. Drug Deliv. Transl. Res. 5, 231–242. https://doi.org/10.1007/s13346-015-0220-8.

Cao, K., Ishida, T., Fang, Y., Shinohara, K., Li, X., Nagaoka, N., Yoshida, T., 2020. Protection of the retinal ganglion cells: Intravitreal injection of resveratrol in mouse model of ocular hypertension. Invest. Ophthalmol. Vis. Sci. 61 (3), 13. https://doi.org/10.1167/iovs.61.3.13.

Cao, Y., Samy, K.E., Bernards, D.A., Desai, T.A., 2019. Recent advances in intraocular sustained-release drug delivery devices. Drug Discov. Today 24 (8), 1694–1700. https://doi.org/10.1016/j.drudis.2019.05.031.

Chaw, S.Y., Novera, W., Chacko, A.M., Wong, T.T.L., Venkatraman, S., 2021. In vivo fate of liposomes after subconjunctival ocular delivery. J. Control. Release 329, 162–174. https://doi.org/10.1016/j.jconrel.2020.11.053.

Cho, J., Heuzey, M.C., Bégin, A., Carreau, P.J., 2006. Viscoelastic properties of chitosan solutions: Effect of concentration and ionic strength. J. Food Eng. 74 (4), 500–515. https://doi.org/10.1016/j.jfoodeng.2005.01.047.

Cui, Q.N., Gray, I.N., Yu, Y., VanderBeek, B.L., 2019. Repeated intravitreal injections of antivascular endothelial growth factors and risk of intraocular pressure medication use. Graefes Arch. Clin. Exp. Ophthalmol. 257, 1931–1939. https://doi.org/10.1007/s00417-019-04362-7.

Drozdova, M.G., Demina, T.S., Dregval, O.A., Gaidar, A.I., Andreeva, E.R., Zelenetskii, A. N., Markvicheva, E., 2022. Macroporous Hyaluronic Acid/Chitosan Polyelectrolyte Complex-Based Hydrogels Loaded with Hydroxyapatite Nanoparticles: Preparation Characterization and in Vitro Evaluation. Polysaccharides 3 (4), 745–760. https://doi.org/10.3390/polysaccharides3040043.

Duda, M., Cygan, K., Wisniewska-Becker, A., 2020. Effects of curcumin on lipid membranes: An EPR spin-label study. Cell Biochem. Biophys. 78, 139–147. https://doi.org/10.1007/s12013-020-00906-5.

Fan, Y., Yue, Z., Lucarelli, E., Wallace, G.G., 2020. Hybrid printing using cellulose nanocrystals reinforced GelMA/HAMA hydrogels for improved structural integration. Adv. Healthc. Mater. 9 (24), 2001410. https://doi.org/10.1002/adhm.202001410.

Farkouh, A., Frigo, P., Czejka, M., 2016. Systemic side effects of eye drops: a pharmacokinetic perspective. Clin Ophthal. 2433–2441 https://doi.org/10.2147/OPTH.S118409.

Forrester, J.V., Kuffova, L., Delibegovic, M., 2020. The role of inflammation in diabetic retinopathy. Front. Immunol. 11, 583687 https://doi.org/10.3389/fimmu.2020.583687.

Fratini, C., Weaver, E., Moroni, S., Irwin, R., Bashi, Y.H.D., Uddin, S., Lamprou, D.A., 2023. Combining microfluidics and coaxial 3D-bioprinting for the manufacturing of diabetic wound healing dressings. Biomater. Adv. 153, 213557 https://doi.org/10.1016/j.bioadv.2023.213557.

García-Estrada, P., García-Bon, M.A., López-Naranjo, E.J., Basaldúa-Pérez, D.N., Santos, A., Navarro-Partida, J., 2021. Polymeric implants for the treatment of intraocular eye diseases: trends in biodegradable and non-biodegradable materials. Pharmaceutics 13 (5), 701. https://doi.org/10.3390/pharmaceutics13050701.

Hammer, S.S., Vieira, C.P., McFarland, D., Sandler, M., Levitsky, Y., Dorweiler, T.F., Busik, J.V., 2021. Fasting and fasting-mimicking treatment activate SIRT1/LXRα and alleviate diabetes-induced systemic and microvascular dysfunction. Diabetologia 64, 1674–1689. https://doi.org/10.1007/s00125-021-05431-5.

Hollborn, M., Chen, R., Wiedemann, P., Reichenbach, A., Bringmann, A., Kohen, L., 2013. Cytotoxic effects of curcumin in human retinal pigment epithelial cells. PLoS One 8 (3), e59603.

Hussein, M.A., El-Maksoud, H.A., 2013. Biochemical effects of resveratrol and curcumin combination on obese diabetic rats. Mol. Clin. Pharmacol. 4 (1), 1–10.

Ishikawa, K., He, S., Terasaki, H., Nazari, H., Zhang, H., Spee, C., Hinton, D.R., 2015. Resveratrol inhibits epithelial-mesenchymal transition of retinal pigment epithelium and development of proliferative vitreoretinopathy. Sci. Rep. 5 (1), 16386. https://doi.org/10.1038/srep16386.

Ismail, E.H., Sabry, D.Y., Mahdy, H., Khalil, M.M.H., 2014. Synthesis and characterization of some ternary metal complexes of curcumin with 1, 10-phenanthroline and their anticancer applications. J. Sci. Res. 6 (3) https://doi.org/10.3329/jsr.v6i3.18750.

Jalili, S., Saeedi, M., 2016. Study of curcumin behavior in two different lipid bilayer models of liposomal curcumin using molecular dynamics simulation. J. Biomol. Struct. Dyn. 34 (2), 327–340. https://doi.org/10.1080/07391102.2015.1030692.

Jaradat, E., Weaver, E., Meziane, A., Lamprou, D.A., 2022. Microfluidic paclitaxel-loaded lipid nanoparticle formulations for chemotherapy. Int. J. Pharm. 628, 122320 https://doi.org/10.1016/j.ijpharm.2022.122320.

Jaradat, E., Weaver, E., Meziane, A., Lamprou, D.A., 2023. Synthesis and characterization of paclitaxel-loaded pegylated liposomes by the microfluidics method. Mol. Pharm. 20 (12), 6184–6196. https://doi.org/10.1021/acs.molpharmaceut.3c00596.

Jervis, L.P., 2017. A summary of recent advances in ocular inserts and implants. J. Bioequiv. Availab. 9, 320–323. https://doi.org/10.4172/jbb.1000318.

Jiang, D., Xu, T., Zhong, L., Liang, Q., Hu, Y., Xiao, W., Shi, J., 2023. Research progress of VEGFR small molecule inhibitors in ocular neovascular diseases. Eur. J. Med. Chem. 115535 https://doi.org/10.1016/j.ejmech.2023.115535.

Khoonkari, M., Es Sayed, J., Oggioni, M., Amirsadeghi, A., Dijkstra, P., Parisi, D., Kamperman, M., 2023. Bioinspired processing: Complex coacervates as versatile inks for 3D bioprinting. Adv. Mater. 35 (28), 2210769. https://doi.org/10.1002/adma.202210769.

Khunmanee, S., Jeong, Y., Park, H., 2017. Crosslinking method of hyaluronic-based hydrogel for biomedical applications. J. Tissue Eng. 8, 2041731417726464 https://doi.org/10.1177/2041731417726464.

Khurana, R.N., Appa, S.N., McCannel, C.A., Elman, M.J., Wittenberg, S.E., Parks, D.J., Yeh, S., 2014. Dexamethasone implant anterior chamber migration: risk factors, complications, and management strategies. Ophthalmology 121 (1), 67–71. https://doi.org/10.1016/j.ophtha.2013.06.033.

Kundu, S.K., Yoshida, M., Shibayama, M., 2010. Effect of salt content on the rheological properties of hydrogel based on oligomeric electrolyte. J. Phys. Chem. B 114 (4), 1541–1547. https://doi.org/10.1021/jp906312f.

Lazaridou, M., Moroni, S., Klonos, P., Kyritsis, A., Bikiaris, D.N., Lamprou, D.A., 2024. 3D-printed hydrogels based on amphiphilic chitosan derivative loaded with levofloxacin for wound healing applications. Int. J. Polym. Mater. 1–18 https://doi.org/10.1080/00914037.2024.2314610.

Le, H.R., Qu, S., Mackay, R.E., Rothwell, R., 2012. Fabrication and mechanical properties of chitosan composite membrane containing hydroxyapatite particles. J. Adv. Ceram. 1, 66–71. https://doi.org/10.1007/s40145-012-0007-z.

Leley, S.P., Ciulla, T.A., Bhatwadekar, A.D., 2021. Diabetic retinopathy in the aging population: a perspective of pathogenesis and treatment. Clin. Interv. Aging 1367–1378. https://doi.org/10.2147/CIA.S297494.

Li, L., Wang, N., Jin, X., Deng, R., Nie, S., Sun, L., Gong, C., 2014. Biodegradable and injectable in situ cross-linking chitosan-hyaluronic acid based hydrogels for postoperative adhesion prevention. Biomaterials 35 (12), 3903–3917. https://doi.org/10.1016/j.biomaterials.2014.01.050.

Liu, X., Shen, W., Xia, W., Lu, P., 2023. Early effects of intravitreal anti-VEGF agents on cornea and visual acuity in patients with diabetic retinopathy. Cutan. Ocul. Toxicol. 42 (4), 213–218. https://doi.org/10.1080/15569527.2023.2234036.

Maiz-Fernández, S., Barroso, N., Pérez-Álvarez, L., Silván, U., Vilas-Vilela, J.L., Lanceros-Mendez, S., 2021. 3D printable self-healing hyaluronic acid/chitosan polycomplex hydrogels with drug release capability. Int. J. Biol. Macromol. 188, 820–832. https://doi.org/10.1016/j.ijbiomac.2021.08.022.

Mare, R., Paolino, D., Celia, C., Molinaro, R., Fresta, M., Cosco, D., 2018. Post-insertion parameters of PEG-derivatives in phosphocholine-liposomes. Int. J. Pharm. 552 (1–2), 414–421. https://doi.org/10.1016/j.ijpharm.2018.10.028.

Martín-López, E., Alonso, F.R., Nieto-Díaz, M., Nieto-Sampedro, M., 2012. Chitosan, gelatin and poly (L-Lysine) polyelectrolyte-based scaffolds and films for neural tissue engineering. J. Biomater. Sci. Polym. Ed. 23 (1–4), 207–232. https://doi.org/10.1163/092050610X546426.

McAvoy, K., Jones, D., Thakur, R.R.S., 2018. Synthesis and characterisation of photocrosslinked poly (ethylene glycol) diacrylate implants for sustained ocular drug delivery. Pharm. Res. 35, 1–17. https://doi.org/10.1007/s11095-017-2298-9.

Mishra, D., Gade, S., Glover, K., Sheshala, R., Singh, T.R.R., 2023. Vitreous humor: composition, characteristics and implication on intravitreal drug delivery. Curr. Eye Res. 48 (2), 208–218. https://doi.org/10.1080/02713683.2022.2119254.

Moiseev, R.V., Kaldybekov, D.B., Filippov, S.K., Radulescu, A., Khutoryanskiy, V.V., 2022. Maleimide-decorated PEGylated mucoadhesive liposomes for ocular drug delivery. Langmuir 38 (45), 13870–13879. https://doi.org/10.1021/acs.langmuir.2c02086.

Moroni, S., Bingham, R., Buckley, N., Casettari, L., Lamprou, D.A., 2023. 4D printed multipurpose smart implants for breast cancer management. Int. J. Pharm. 642, 123154 https://doi.org/10.1016/j.ijpharm.2023.123154.

Naageshwaran, V., Ranta, V.P., Toropainen, E., Tuomainen, M., Gum, G., Xie, E., Del Amo, E.M., 2022. Topical pharmacokinetics of dexamethasone suspensions in the rabbit eye: Bioavailability comparison. Int. J. Pharm. 615, 121515 https://doi.org/10.1016/j.ijpharm.2022.121515.

Nakagawa, H., Kiyozuka, Y., Uemura, Y., Senzaki, H., Shikata, N., Hioki, K., Tsubura, A., 2001. Resveratrol inhibits human breast cancer cell growth and may mitigate the effect of linoleic acid, a potent breast cancer cell stimulator. J. Cancer Res. Clin. Oncol. 127, 258–264. https://doi.org/10.1007/s004320000190.

Nedzvetsky, V.S., Gasso, V.Y., Agca, C.A., Sukharenko, E.V., 2021. Soluble curcumin ameliorates motility, adhesiveness and abrogate parthanatos in cadmium-exposed

retinal pigment epithelial cells. Biosyst Divers. 29 (3), 235–243. https://doi.org/10.15421/012129.

Rafael, D., Guerrero, M., Marican, A., Arango, D., Sarmento, B., Ferrer, R., Schwartz Jr, S., 2023. Delivery Systems in Ocular Retinopathies: The Promising Future of Intravitreal Hydrogels as Sustained-Release Scaffolds. Pharmaceutics 15 (5), 1484. https://doi.org/10.3390/pharmaceutics15051484.

Roh, M., Lee, N. G., & Miller, J. B. 2018, January. Complications assoicated with MIRAgel for treatment of retinal detachment. In Semin Ophthalmol., 33 (1), 89-94. Taylor & Francis. https://doi.org/10.1080/08820538.2017.1353822.

Sahu, A.K., Mishra, A.K., 2021. Curcumin-induced membrane property changes in DMPC multilamellar vesicles and the effects of membrane-destabilizing molecules on curcumin-loaded multilamellar vesicles. Langmuir 37 (43), 12753–12766. https://doi.org/10.1021/acs.langmuir.1c02407.

Sigford, D.K., Reddy, S., Mollineaux, C., Schaal, S., 2015. Global reported endophthalmitis risk following intravitreal injections of anti-VEGF: a literature review and analysis. Clin. Ophthalmol. 773–781 https://doi.org/10.2147/OPTH.S77067.

Sommonte, F., Weaver, E., Mathew, E., Denora, N., Lamprou, D.A., 2022. In-house innovative "diamond shaped" 3D printed microfluidic devices for lysozyme-loaded liposomes. Pharmaceutics 14 (11), 2484. https://doi.org/10.3390/pharmaceutics14112484.

Tamam, H., Park, J., Gadalla, H.H., Masters, A.R., Abdel-Aleem, J.A., Abdelrahman, S.I., Yeo, Y., 2019. Development of liposomal gemcitabine with high drug loading capacity. Mol. Parm. 16 (7), 2858–2871. https://doi.org/10.1021/acs.molpharmaceut.8b01284.

Tan, G., Ioannou, N., Mathew, E., Tagalakis, A.D., Lamprou, D.A., Yu-Wai-Man, C., 2022. 3D printing in Ophthalmology: From medical implants to personalised medicine. Int. J. Pharm. 625, 122094 https://doi.org/10.1016/j.ijpharm.2022.122094.

Tavakoli, S., Peynshaert, K., Lajunen, T., Devoldere, J., Del Amo, E.M., Ruponen, M., Urtti, A., 2020. Ocular barriers to retinal delivery of intravitreal liposomes: Impact of vitreoretinal interface. J. Control. Release 328, 952–961. https://doi.org/10.1016/j.jconrel.2020.10.028.

Weaver, E., O'Hagan, C., Lamprou, D.A., 2022. The sustainability of emerging technologies for use in pharmaceutical manufacturing. Expert Opin. Drug Deliv. 19 (7), 861–872. https://doi.org/10.1080/17425247.2022.2093857.

Weaver, E., Macartney, R.A., Irwin, R., Uddin, S., Hooker, A., Burke, G.A., Lamprou, D. A., 2024. Liposomal encapsulation of amoxicillin via microfluidics with subsequent investigation of the significance of PEGylated therapeutics. Int. J. Pharm. 650, 123710 https://doi.org/10.1016/j.ijpharm.2023.123710.

Wiciński, M., Erdmann, J., Nowacka, A., Kuźmiński, O., Michalak, K., Janowski, K., Zabrzyński, J., 2023. Natural phytochemicals as SIRT activators—focus on potential biochemical mechanisms. Nutrients 15 (16), 3578. https://doi.org/10.3390/nu15163578.

Yang, Y., Duan, W., Lin, Y., Yi, W., Liang, Z., Yan, J., Jin, Z., 2013. SIRT1 activation by curcumin pretreatment attenuates mitochondrial oxidative damage induced by myocardial ischemia reperfusion injury. Free Radic. Biol. Med. 65, 667–679. https://doi.org/10.1016/j.freeradbiomed.2013.07.007.

Zhang, X., Wei, D., Xu, Y., Zhu, Q., 2021. Hyaluronic acid in ocular drug delivery. Carbohydr. Polym. 264, 118006 https://doi.org/10.1016/j.carbpol.2021.118006.

Zingale, E., Rizzo, S., Bonaccorso, A., Consoli, V., Vanella, L., Musumeci, T., Pignatello, R., 2022. Optimization of lipid nanoparticles by response surface methodology to improve the ocular delivery of diosmin: characterization and in-vitro anti-inflammatory assessment. Pharmaceutics 14 (9), 1961. https://doi.org/10.3390/pharmaceutics14091961.

Zingale, E., Bonaccorso, A., D'Amico, A.G., Lombardo, R., D'Agata, V., Rautio, J., Pignatello, R., 2024. Formulating resveratrol and melatonin self-nanoemulsifying drug delivery systems (SNEDDS) for ocular administration using design of experiments. Pharmaceutics 16 (1), 125. https://doi.org/10.3390/pharmaceutics16010125.